ARTICLE OPEN

Check for updates

Dynamical downfolding for localized quantum states

Mariya Romanova [1], Guorong Weng [1], Arsineh Apelian[2] and Vojtěch Vlček [1,2]✉

We introduce an approach to treat localized correlated electronic states in the otherwise weakly correlated host medium. Here, the environment is dynamically downfolded on the correlated subspace. It is captured via renormalization of one and two quasiparticle interaction terms which are evaluated using many-body perturbation theory. We outline the strategy on how to take the dynamical effects into account by going beyond the static limit approximation. Further, we introduce an efficient stochastic implementation that enables treating the host environment with a large number of electrons at a minimal computational cost. For a small explicitly correlated subspace, the dynamical effects are critical. We demonstrate the methodology by reproducing optical excitations in the negatively charged NV center defect in diamond, that agree with experimental results.

INTRODUCTION

The ability to predict and computationally tackle electronic excitations is key for guiding the development of new materials in many areas ranging from quantum technologies to ultrafast electronics. In this context, materials hosting strongly coupled electronic states are particularly interesting, but they pose a significant challenge to theory. Despite the great progress in making explicitly correlated computational approaches more affordable[1–8], calculations are still limited to problems with a small number of quantum particles. Fortunately, the most important contribution is, in many cases, limited to only a small range of electronic states, i.e., a subspace of the system. A common approach to alleviate the computational cost is to invoke theoretical treatment[9–17] in which a small explicitly correlated problem (solvable computationally) is embedded in the remaining portion of the system, which is treated at a more approximate level.

In practice, the calculations have to deal with a number of methodological bottlenecks that can compromise the accuracy of the model. Determining the correlated subspace is not always straightforward and often based on chemical or physical intuition. Further, the strongly interacting states are coupled to the rest of the system[6], i.e., the remaining (weakly interacting) electrons are influenced by the electronic configuration of the subspace and self-consistent treatment is thus required[18,19]. Moreover, the extent of the dynamical coupling depends on the size of the explicitly correlated region; in other words: the larger the correlated region is, the more dynamical interactions are treated explicitly and the simpler the coupling to the rest of the system is. The importance of the dynamical renormalization has been recognized[20–24] and the constrained random phase approximation (cRPA) has become a de facto standard in accounting for the dynamics of the environment outside of the correlated subspace[14,15,25–27]. For technical reasons, a static limit approximation is ubiquitously applied, instead of the fully dynamical description[16,17,28], and cRPA calculations are computationally prohibitive for large systems[29].

Here, we combine an efficient stochastic cRPA (s-cRPA)[29] approach and describe a complementary strategy in which the weakly interacting environment is downfolded on the correlated subspace and the dynamical interactions are fully taken into account. In analogy to the approaches considering individual quasiparticles (QPs), the majority of the system (i.e., the environment) is captured via effective single- and two-QP interactions within the subspace. The dynamical response of the weakly correlated electrons is captured by renormalized interaction terms, whose dynamics compensate for the reduced subspace dimensionality. We extend the previously developed stochastic cRPA[29] to arbitrary two-body couplings. More fundamentally, we provide a tractable construction of the downfolded (and therefore frequency dependent) Hamiltonian treating strongly correlated subspace of interacting QPs. The frequency-dependence of the one and two-body terms is circumvented by solving a set of auxiliary QP propagator problems, which determine at which frequencies the dynamical interactions enter the many-body Hamiltonian. We suggest a practical (approximate) choice for the propagators and discuss avenues to generalize this methodology further (e.g., in cases when particle-particle scattering or electron-phonon couplings are important).

We exemplify the approach by reproducing the experimentally measured optical excitations in a single NV^- defect center in diamond. The defect consists of a small number of correlated states (requiring an explicitly correlated method), formed by dangling bonds pointing toward the vacancy. This subspace definition is physically and chemically motivated. The remaining host environment is weakly correlated: diamond's fundamental and optical band gaps are well reproduced within many-body perturbation theory (MBPT) already at the level of G_0W_0[30–32] and BSE[33,34], suggesting that MBPT is sufficient for the electronic dynamics and the related downfolding. Further, we employ stochastic formalism that is applicable to large scale systems. The optical excitations obtained by the stochastic dynamical downfolding approach agree with experimental measurements. While beyond the scope of this work, the proposed method serves as a starting point to compute other quantities and observables. For instance, the spectral function for the correlated subspace is obtained from the one-QP Green's function (GF) using the correlated Hamiltonian, as detailed e.g., in ref. [35].

[1]Department of Chemistry and Biochemistry, University of California, Santa Barbara, CA 93106-9510, USA. [2]Department of Materials, University of California, Santa Barbara, CA 93106-9510, USA. ✉email: vlcek@ucsb.edu

RESULTS AND DISCUSSION

Stochastic *GW* in weakly correlated host material

We first analyze the QP band gap of pristine diamond and compare it to one of the defect supercells. Details about the convergence of the band gap with respect to the system size are available in Section "Implementation". Our stochastic G_0W_0 calculations of a 4096-atom diamond supercell provide a QP band gap of the 5.6 eV. This is consistent with our previous calculations[30]. Further, for the defect center, the subset of localized defect states have been extensively tested in our earlier work[36] and showed that 511-atom cell provides converged results. The G_0W_0 calculations of a 511-atom diamond supercell containing the NV^{-1} defect provide a band gap of 5.3 eV. While the relaxed supercells hosting NV^{-1} center are distinct from the pristine (ideally periodic) diamond structure, we found that the 511-atom cell has a gap less than 0.1 eV away from the ideal 512-atom diamond cell[30]. Both results are in good agreement with the experimental value of 5.5 eV[37]. Note that the G_0W_0 results are generally in good agreement with experimental band gaps. This is true even though the electron-phonon band gap renormalization is neglected (and has a profound effect as shown independently by several authors[38,39], and others). In the same vein, it is reasonable to assume that a similar error cancellation will occur for dynamical downfolding based on G_0W_0 and RPA, and that it will also perform well and match experimental zero-phonon optical transitions. However, in general, when electron-phonon interactions are important, Σ^{env} needs to account for these scattering mechanisms, e.g., as alluded to in Section "Methods".

Dynamically downfolded effective Hamiltonian

We now turn to the analysis of the QP energies of the defect defined by the maximally localized states. Treating the defect states at the G_0W_0 level leads to a small difference between the individual sites (Fig. 1), i.e., they are energetically similar with a difference of merely 0.51 eV for the orbitals located on nitrogen and carbon atoms. Note that at this point all electrons, including those in the correlated subspace, are described by the G_0W_0 self-energy.
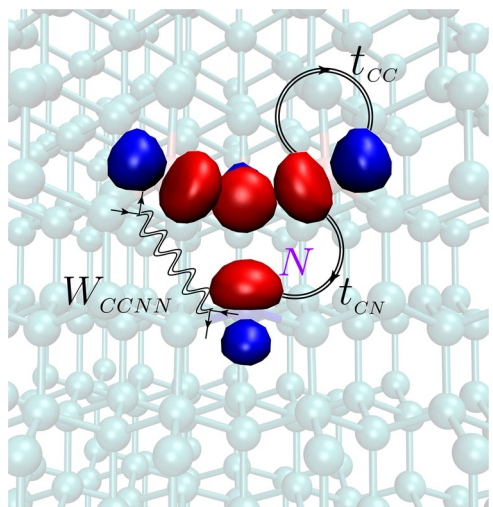

Fig. 1 Model representation of the NV⁻. Three carbon sites are on top and nitrogen site at the bottom. Maximally localized single particle states are shown by isosurface plots: red and blue colors represent positive and negative value of a real valued orbitals. Examples of one- and two-body terms are depicted diagrammatically. The one-body terms (*t*) are obtained from single QP propagators renormalized by the self-energy of the environment. The two-body terms (*W*) contain screened Coulomb interactions.

The first step in solving the correlated problem is to project the electronic structure onto a selected subspace of states treated by an explicitly correlated effective Hamiltonian:

$$\hat{H} = -\sum_{i,j,\sigma} t_{ij}\hat{c}_{i\sigma}^\dagger \hat{c}_{j\sigma} + \frac{1}{2}\sum_{ijkl\sigma\sigma'} W_{ijkl}\hat{c}_{i\sigma}^\dagger \hat{c}_{j\sigma'}^\dagger \hat{c}_{l\sigma'} \hat{c}_{k\sigma}, \quad (1)$$

where $\hat{c}_{i\sigma}^\dagger$ and $\hat{c}_{i,\sigma}$ are creation and annihilation operators in site i with spin σ. t_{ij} represents the one-body term capturing individual QPs within the subspace. The term is conventionally separated into the on-site, $i = j$, and hopping, $i \neq j$, amplitudes. The t terms are computed as $t_{ij} = \langle i|H_{qp}^{env}|j\rangle$ using a single-QP Hamiltonian, H_{qp}^{env}, containing the downfolded interactions from the environment. The second term, W_{ijkl}, describes two-body (i.e., explicit QP-QP) interactions within the subspace renormalized by the environment (i.e., the electronic states outside of the correlated problem). Details about the calculations of one- and two-body terms are provided in Methods. In this formulation, the GW treatment corresponds to "downfolding" on individual independent QPs, whose energies are determined by H_{qp} containing interactions from the entire system, i.e., there is no distinct treatment of the environment and the subspace. In this limit, the QPs in the subspace are computed by the same approach as the environment, corresponding to a "GW in GW" calculation that enables formal decomposition of H_{qp} to the "environment" and "defect" contributions as illustrated already in ref. [40]. For completeness, this decomposition is also shown in Supplementary Fig. 7.

Here, we analyze the individual one-body (single QP) t terms entering the Eq. (1) and computed with Eq. (8). In contrast to the G_0W_0 QP energies discussed above, calculations of t terms are based on screened interactions and also contain only a portion of the exchange-correlation self-energy. The difference between the t_{ii} terms for the N and C sites becomes significantly larger (12.7 eV). This is because the response of the environment to the localized QPs is not balanced by the induced fluctuation of the particles in the localized states (i.e., only the response of the environment is included in the t terms). This value should be contrasted with the estimate of the t terms neglecting the Σ^{env} term of Eq. (8) (19.9 eV), which represents a simplified version of the onsite energy (that contains only kinetic and ionic potential) applied in previous studies[41,42]. In this case, it thus seems that the environmental contributions are significantly renormalizing the trivial contribution to the differences between the subspace sites. In the effective Hamiltonian, the differences between the onsite t terms are critical to determining the triplet-triplet transition (c.f., Supplementary Note 1). Here, we analyze the individual one-body (single QP) t terms entering the Eq. (1) and computed with Eq. (8). In contrast to the G_0W_0 QP energies discussed above, calculations of t terms are based on screened interactions and also contain only a portion of the exchange-correlation self-energy. The difference between the t_{ii} terms for the N and C sites becomes significantly larger (12.7 eV). This is because the response of the environment to the localized QPs is not balanced by the induced fluctuation of the particles in the localized states (i.e., only the response of the environment is included in the t terms). This value should be contrasted with the estimate of the t terms neglecting the Σ^{env} term of Eq. (8) (19.9 eV), which represents a simplified version of the onsite energy (that contains only kinetic and ionic potential) applied in previous studies[41,42]. In this case, it thus seems that the environmental contributions are significantly renormalizing the trivial contribution to the differences between the subspace sites. In the effective Hamiltonian, the differences between the onsite t terms are critical to determining the triplet-triplet transition (c.f., Supplementary Note 1). When inspecting the matrix of t elements, including the intersite hopping (t_{ij}), we notice that the maximally localized basis is strongly diagonally dominant and the t_{ij} are on average just 6% of the t_{ii} terms (0.74 eV on
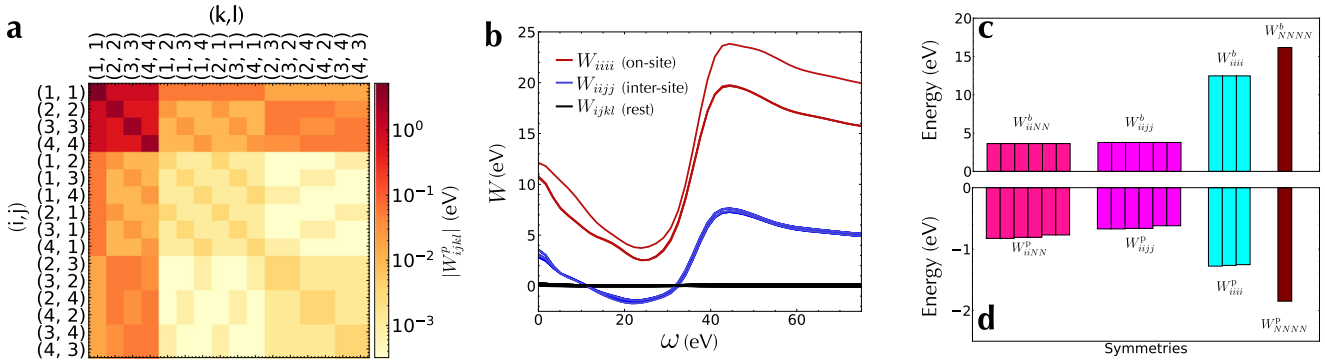
Fig. 2 Parameters of the downfolded Hamiltonian. a Color map of absolute values of the screening part of all 256 interaction parameters estimated at the static limit $W_{ijkl}^{p}(\omega = 0)$. **b** Frequency dependence of the total bare plus screened interaction for 3200 stochastic samples. Interaction terms are highlighted by color according to the physical meaning. Red represents the on-site Coulomb interaction terms, blue - inter-site, black - all remaining interaction terms. Stochastic errors are smaller than the line thickness. **c** Bare Coulomb on-site and inter-site parameters $W_{iiii,iijj}^{b}$. **d** Screening part of the Coulomb parameters after retaining the hermitian part of the interactions $W_{iiii,iijj}^{p}(\omega = 0)$. Computed with 3200 stochastic samples in the 511-atom cell. In **c** and **d** parameters obeying the same symmetry operations are highlighted with the same color.

average). Further, the dependence of the t terms on ω is relatively weak and slowly varying. If the dynamical effects are neglected in the Hartree term (i.e., taking the static limit of Σ_{H}^{env}), we recover the difference of 15.2 eV between the onsite single-QP terms for N and C orbitals. Here, the renormalization decreases by roughly 35%, while much of the remaining difference stems from the dynamical contribution of Σ_{xc}^{env}.

Next we analyze the results for the two-body interactions, W_{ijkl}, defined in this work in a following notation: $W_{ijkl} = \int \varphi_i^*(\mathbf{r})\varphi_j(\mathbf{r})W(\mathbf{r},\mathbf{r}')\varphi_k^*(\mathbf{r}')\varphi_l(\mathbf{r}')d\mathbf{r}d\mathbf{r}'$. Figure 2a shows the values of interaction parameters at the static limit $W^{p}(\omega = 0)$ on a color map. By ordering the (i, j) and (k, l) indices, we group together the dominant on-site and inter-site density-density interactions that appear in the left top corner, i.e., W_{iiii}^{p} and W_{iijj}^{p}. The remaining terms do not exceed 70 meV (both bare and screened); this is true for all frequencies as we show in Fig. 2b (black curves). The convergence of the four dominant parameters with samplings as a function of supercell size is provided in Supplementary Fig. 4. In the rest of this work, we exclude all the terms with a magnitude of <70 meV.

Note that the minimal model preserves the C_{3v} symmetry, which is also satisfied by the underlying mean-field Hamiltonian. However, the statistical sampling is associated with finite stochastic errors and the corresponding interaction symmetry is restored *a posteriori*. In particular, the bare component, W_{ijkl}^{b}, naturally preserves symmetry under the permutation of indices $ijkl \leftrightarrow klij$. In general, this is not satisfied for stochastically sampled polarization part, W_{ijkl}^{p}, (cf. Supplementary Fig. 5) which would translate to level splitting (of otherwise degenerate excitations) in the optical spectrum of the NV^{-}.

To recover the expected behavior we enforce the individual symmetries; in practice, this is analogous to the Hermitization of the QP Hamiltonian as in refs. [29,43,44]:

$$W_{ijkl}^{p}(\omega) = \frac{1}{4}[W_{ijkl}^{p}(\omega) + W_{klij}^{p*}(\omega) + W_{klij}^{p}(\omega) + W_{ijkl}^{p*}(\omega)] \quad (2)$$

Figure 2d demonstrates the converged result of $W_{ijkl}^{p}(\omega)$ with 3200 samplings. There however remains a finite difference within each group of elements on the order of 20 meV, attributed to numerical artifacts. This small symmetry breaking leads to errors much lower than the practical resolution determined by the sampling error for individual QP levels which is at most ~54 meV. In the following, we use 3,200 samplings as they lead to a reasonable balance between the computational cost and accuracy. The statistical error is at least 30% smaller than the magnitude of the smallest values of $W_{ijkl}(\omega)$ (shown by the black

line in Fig. 2b) that contribute negligibly to the results reported here. We report the splitting in Supplementary Table I for each supercell size. In the rest of this work, we average the screened counterpart of the interaction parameters within each symmetry group (depicted in Fig. 2d for the four cases considered).

Figure 2b depicts the frequency dependence of $W_{ijkl}(\omega)$ terms. The magnitude of the response depends on the localization of a perturbation, e.g. the more delocalized the perturbing state is (i.e. if the canonical Kohn Sham defect state is used instead of more localized wannier), the weaker the response (test performed in this work, shown in the Supplementary Fig. 6). In contrast to the slowly varying frequency dependence of t terms, the frequency dependence of the two-body interactions is more pronounced. The renormalization is caused by the response due to the charge dipole fluctuations. Therefore, the values of W_{ijkl} are determined at excitation energies ω_{2qp} obtained from the fixed point solution for the particle-hole propagator in the environment. Specifically, we solve a two-QP Hamiltonian H_{2qp} associated with the poles of the two-QP propagator satisfying the Bethe-Salpeter equation (BSE), see details in Section "Methods" Eq. (10); The frequency ω_{2qp} represents an auxiliary BSE solution for a particular pair of QPs. The corresponding renormalized two-body interactions are evaluated at ω_{2qp}. Note that these excitations only define the energy scales of the W terms and do not directly translate to excitations of the explicitly correlated many-body states in the subspace, i.e. to the optical spectrum we seek. For further details and the approximations employed see Section "Methods". For the optical transition between two C sites, we obtain a value of 2.3 eV while between N and C site a value of 2.6 eV. The energy significantly increases, if excitation is confined to be in between two states on a single site (6.3 and 7.7 eV on the C and N sites). Compared to the bare interactions, the dynamically screened $W_{iiii}(\omega_{2qp})$ are decreased by as much as 52% for N and 50% for the C sites. The intersite density-density is lower by 38% between two C sites, and by 29% for those between N and C sites. This significant change can be deduced from the steep dependence of $W(\omega)$ curves in Fig. 2b. As mentioned above, the remaining terms have small magnitudes and are neglected. Taking the static limit of $W(\omega)$ leads to a much weaker screening, especially for the "on-site" (W_{iiii}) terms, which are reduced by 23% and 20% for N and C sites. In contrast, the intersite terms (W_{iijj}) are reduced by 22% between N and C and by 18% between two C sites. Regardless of the approach, considering the dynamical effects away from the static limit leads to a reduction of the two-body interaction strength compared to considering the limit $\omega \to 0$ (see Supplementary Note 1). This does not necessarily mean that the system becomes more weakly
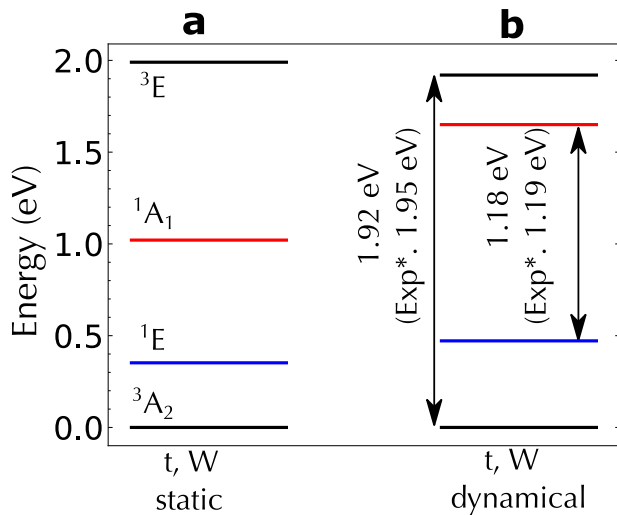
Fig. 3 Excited states on the NV⁻. Comparison of the excited states of the NV⁻ center in 511 atom supercell where the electron-electron interaction parameters were computed in this work with **a** t and W screened within stochastic s-cRPA at static limit $\omega = 0$ **b** both t and W are dynamically renormalized; Number of stochastic samples $N_{|\tilde{\eta}|} = 3200$. (*) Note, experimental values of zero phonon lines are presented on the plot, while our results are computed for vertical excitations.

interacting. In fact, the degree of electronic correlation can be paralleled with the presence of multiple excitation channels competing at similar energy scales[35] and, indeed, it was shown in the context of DMFT that the inclusion of dynamical effects tends to increase the apparent strength of electronic correlations[23,24].

Excitation energies of the dynamically downfolded model

In the final step, we study the excitation energies obtained by exact diagonalization of Eq. (1) within the minimal subspace defined by the localized orbitals with the parameters t and W fixed at ω_{qp} and ω_{2qp} correspondingly. We consider the fully dynamically renormalized case and compare it to the corresponding static limits. In the latter, the one-body terms contain the contribution of Σ_{xc}^{env} computed at the single-QP excitation energy (in analogy to the G_0W_0 approximation), but the dynamics of the Hartree term is neglected as we take $\lim_{\omega \to 0} \Sigma_H^{env}(\omega)$. Similarly, the two-body interaction in the static limit is $\lim_{\omega \to 0} W_{ijkl}(\omega)$. Figure 3 shows the comparison of the two sets of results. Note, since the hermicity is imposed on the many-body Hamiltonian (as an additional approximation), both t and W parameters are also required to be symmetric (see Eqs. (2) and (9)). Therefore the current approximation does not provide life-times of the excited states, in general, however, the downfolding provides information on life-times.

The triplet-triplet vertical transition, $^3E \leftrightarrow {}^3A_2$, is not substantially different for the two limiting cases. Based on the analysis of the simple effective Hamiltonian for the NV⁻ center (see Supplementary Note 1), we expect that the triplet transitions are largely determined by the differences between the onsite one-body terms t. While the dynamical effects change them by roughly 20%, the resulting optical excitation spacing is insensitive to such a change. The static and the dynamically screened limits yield values of 1.98 and 1.92 eV which agree with the experimental zero-phonon excitation of 1.95 eV[45].

Our result compares well to previous theoretical works that employed embedding methods despite major differences in the theory. For instance, values of 2.02 eV and 2.05 eV of the triplet-triplet transition were obtained in refs. [25,27] using the quantum

defect embedding theory. These approaches employ a hopping term described at the DFT level and the two-body interaction parameters computed with cRPA in the static limit. A double counting error, i.e., a spurious inclusion of (a portion of) the correlated subspace in the calculation for the environment, arises in embedding approaches[15,25,27]. (It is circumvented in this work by separation of the self-energy). This is especially problematic for embedding within DFT; in refs. [25,27] an approximate Hartree-Fock double counting correction scheme was employed. More recent work[15] formulated an exact double counting correction for G_0W_0, combined with cRPA treatment of the two-body interactions at the static limit. We surmise that this $\omega \to 0$ formulation translates into a much larger subspace size requirement (indeed, the converged subspace required 12 orbitals, 22 electrons). Ultimately, the converged value for the triplet-triplet transition in ref. [15] was estimated to be 2.15 eV.

The dynamical effects turn out more critical for the singlet-singlet $^1A_1 \leftrightarrow {}^1E$ excitations, which are more sensitive to the relative magnitude of the W terms. As mentioned above, the screening significantly decreases the magnitude of W_{ijkl}. This is illustrated in the Supplementary Note 1 and also discussed in more detail below. We see that in the static case, the singlet-singlet transition is 0.7 eV, which is lower than 1.19 eV the zero-phonon line observed experimentally[46]. These results are in good agreement with other published cRPA results in the static limit. Specifically, a value of 0.8 eV was obtained in refs. [15,27], though this can be improved if beyond cRPA response is used[14].

In contrast, our result for the fully dynamical renormalization of single-singlet transition is 1.18 eV (at s-cRPA level) agrees with the experiment. This is largely due to the reduction of the two-body terms when the dynamics of the density fluctuations is fully taken into account. As noted above, we made a particular choice of H_{2qp} while a different formulation may change the results as the QP-QP interactions would be evaluated at distinct values of ω_{2qp}. Nevertheless, the interaction term is reduced at a finite frequency compared to the static limit, and this leads to improved singlet-singlet transition energy (See Supplementary Fig. 2). This step clearly illustrates that going beyond the typical static limit improves the results appreciably.

A prototypical embedding method applied to periodic correlated systems is the dynamical mean field theory (DMFT). Here, the correlated subspace is coupled to the bath of the bosonic degrees of freedom which represents the interaction with the rest of the system. In contrast, the downfolding captures the problem via a chosen correlated subspace while the host material is represented via the dynamical effect entering each interaction term. This can be paralleled with a lossless compression: the information about the entire system is fully reconstructed through the dynamical one and two-body terms. For weakly correlated host systems (which are accurately treated via MBPT) our strategy offers a great computational advantage. The downfolding approach mitigates a need for a self-consistent solution, represented by a matching condition between the correlated subspace and the bath degrees of freedom in DMFT. While the dynamical downfolding method is general and widely applicable, it also has some limitations, such as the intractability of exact diagonalization for large-scale subspaces and the approximations involved in the MBPT treatment of the environment. In the latter case, it is possible to employ the renormalization group (RG) approach[8], offering a complementary route to extract the response of the system to the QPs in the subspace (via "lossy" compression). This direction will be explored in the future. Yet, the efficiency of the stochastic dynamical downfolding approach suggests that it is a practical and reliable methodology for treating localized correlated phenomena (such as quantum defects and beyond).

Indeed, the results for the negatively charged NV center in bulk diamond practically demonstrate that the dynamically downfolded representation agrees with the experimental excited

energies of the defect. We believe that this is a jumping-off point for future practical simulations of electronic excitations in localized quantum states.

METHODS

The t and W terms of Eq. (1) critically depend on the definition of the correlated space and the projection onto it effectively lowers the problem dimensionality. It is exact provided that both one- and two-body terms downfold all the interactions with the remainder of the system[28]. Further, it requires solving a non-linear eigenvalue problem of the frequency-dependent Hamiltonian. Here, we provide a route to bypass the problem by solving a set of auxiliary QP propagator equations, which determine the frequencies at which the one- and two-QP terms enter the many-body Hamiltonian. We consider only electronic degrees of freedom; the downfolded representation thus captures the coupling with the electronic states (i.e., the charge and configuration fluctuations) outside of the subspace treated by Eq. (1). In particular, we consider the charge density and exchange-correlation interactions. Both contributions include dynamical induced effects (e.g., polarization) and higher order terms described e.g., in Ref. [47] and hence renormalize the t and W terms[28]. To the lowest order, the induced interactions include induced charge density fluctuations. In general, they also contain an induced density matrix[47,48]. Note that if the dynamics of the subspace problem is artificially decoupled from the environment (i.e., only static interactions are considered), the exact solution requires a self-consistent re-evaluation of the one- and two-body terms to reflect the induced effects. Such a self-consistency is circumvented in the (dynamical) downfolding approach shown here.

Clearly, the size of the explicitly correlated region and its coupling to the remainder of the system determines the degree of dynamical effects that needs to be captured by t and W. In this work, we seek only the minimal configuration space, obtained by localizing the electronic states on the atoms neighboring the defect (Fig. 1), and explore the role of dynamical renormalization of individual terms entering Eq. (1). This leads to only four, physically motivated, orbitals in which the QPs are renormalized by the environment of weakly correlated electrons in diamond. The practical calculations thus need to address how to determine such terms and how (i.e., at which frequency) they enter the Hamiltonian.

The downfolding derives directly from the single QP equation of motion:

$$i\partial_{t_1} G(1,2) = \delta(1,2) + h_0(1)G(1,2) - iv(1^+,\overline{3})L(1,\overline{3},2,\overline{3}^+), \quad (3)$$

where G is the one-body Green's function (GF) defined as $G(1,2) = -i\langle N|\mathcal{T}[\hat{c}(1)\hat{c}^\dagger(2)]|N\rangle$ with time-ordering operator $\mathcal{T}$ and $|N\rangle$ representing the N-particle many-body ground state. Here, the GF is defined using the 0K formalism, however, it can be generalized to a finite temperature via the thermal quantum field formalism. Further, $h_0 = \hat{T} + \hat{V}^{ext}$ is the one-particle operator composed of the kinetic and external (ionic) potential terms, v is the bare Coulomb interaction, and L is the two-particle Green's function defined as a time ordered product of two creation and two annihilation operators (i.e., analogously to G). We adopted the shorthand notation for space-time coordinates, i.e., $1 \equiv r_1, t_1$, and bar indicates a coordinate to be integrated over. In MBPT, the two-body interactions are downfolded by introducing Hartree and exchange-correlation self-energies:

$$v(1^+,\overline{3})L(1,\overline{3},2,\overline{3}^+) = \Sigma_H(1,\overline{3})G(1,2) + \Sigma_{xc}(1,\overline{3})G(\overline{3},2). \quad (4)$$

The Hartree self-energy, Σ_H, is the potential due to the density mediated by the instantaneous Coulomb term $\Sigma_H(1,\overline{3}) = v(1,\overline{3})G(\overline{3},\overline{3}^+)$ and $v(1,2) = (|r_1 - r_2|)^{-1}\delta(t_1 - t_2)$. Σ_{xc} downfolds all quantum two-body effects not included in Σ_H (discussed later

and, e.g., in ref. [28]). The QP dynamics is governed by excitation energies, corresponding to poles of G in the frequency domain; these are represented as eigenvalues of the effective QP Hamiltonian $H^{qp} = \hat{T} + \hat{V}^{ext} + \hat{\Sigma}(\omega)$, where the total self-energy, Σ, is frequency dependent as a result of Fourier transformation from the time domain. For a particular QP state, H^{qp} is computed as a fixed point equation with Σ evaluated at ω corresponding to the QP energy.

We now discuss the calculations of t and W terms, which follow a similar route with the important difference, that only the interactions with electrons in the remainder of the systems (i.e., outside of the correlated subspace) are downfolded. Given the constrained description with fixed minimal orbital space, localizing a QP in a particular state ϕ_j is associated with charge fluctuation inside the subspace and polarization of the environment ($P^{env} = \chi^{env}v$). Here, the superscript "env" indicates that the polarization is restricted to the environment part of the system. The separation into subspaces is based on state selection (and not on e.g., spatial coordinates). Further, note that similarly to ref. [15] we assume the interaction between the subspace and the environment is negligible. Indeed, we have tested this hypothesis and the overall results differ by $< 1\%$ (see Section "Implementation"). The notation used is described in the SI. The QPs in the subspace thus interact via a renormalized (screened) Coulomb interaction:

$$W^{env}(1,2) = v(1,2) + v(1,\overline{3})\chi^{env}(\overline{3},\overline{4})v(\overline{4},2), \quad (5)$$

where χ^{env} is the reducible polarizability of the environment due to a potential variation δU: $\chi^{env} = \delta n^{env}/\delta U$, where δU is in the subspace that is "external" to the environment. Within the GF formalism, the two-particle interactions are formally downfolded by substituting v terms by W^{env}.

It is now important to distinguish interactions within the subspace and with the remainder of the system. For a pair or QPs inside the correlated region, we consider explicit interactions mediated by the renormalized W^{env}. Hence, for a particular choice of localized single-QP states $\{\phi\}$, we obtain a dynamical two-body term as:

$$W_{ijkl}(\omega) = \left\langle \phi_i\phi_j|\hat{W}^{env}(\omega)|\phi_k\phi_l \right\rangle, \quad (6)$$

which enters Eq. (1).

For the one-body term, the single-QP dynamics is governed by Eq. (3) with downfolded two-body interactions between electrons inside and outside the correlated subspace. We require, that the same formalism applies (formally) to all states, i.e., the two-body interactions represented by L will be mediated by W^{env}. We thus write:

$$\begin{aligned} W^{env}(1^+,\overline{3})L(1,\overline{3},2,\overline{3}^+) \\ = \Sigma_H^{env}(1,\overline{3})G(1,2) + \Sigma_{xc}^{env}(1,\overline{3})G(\overline{3},2), \end{aligned} \quad (7)$$

where $\Sigma_H^{env}(1,\overline{3}) = W^{env}(1,\overline{3})G^{env}(\overline{3},\overline{3}^+)$ is a dynamical Hartree term which includes the effect of induced charge density in the environment, represented by $G^{env}(1,1^+)$, caused by density fluctuations inside the subspace. This is a single-QP term, the physical meaning of which is to account for the propagation of a single QP in the local Hartree potential of other electrons. Note, the localization of a quasiparticle on a particular site or its hopping (corresponding to terms t_{ii} and t_{ij} accordingly) are associated with different QP energies and charge fluctuations. Thus, they are subject to distinct local potentials. Similarly, the exchange correlation term is, in general, $\Sigma_{xc}^{env}(1,2) = G^{env}(1,\overline{3})W^{env}(1^+,\overline{4})\overline{\Gamma}^{env}(\overline{3},\overline{4},2)$, where the GF is constructed only from the states of the environment. Note, both Hartree and exchange correlation self-energies are restricted to the states of the environment to avoid double counting in the subspace. The vertex $\overline{\Gamma}^{env} = \delta(G^{env})^{-1}/\delta U$ is constructed from the response of the environment to the variation of the "external" potential δU. Note that the vertex is reducible, i.e., distinct from the

counterpart typically encountered in the Hedin's formalism[28,48,49]. In practice, this means that an additional screened response needs to be included in the self-energy expansion given that Eq. (7) substitutes v with W^{env}.

Using the combined self-energy $\Sigma^{env} = \Sigma_H^{env} + \Sigma_{xc}^{env}$, based on the quantities defined in Eq. (7), we obtain the single-QP effective Hamiltonian containing the renormalization effects stemming from the environment: $H_{qp}^{env} = \hat{T} + \hat{V}^{ext} + \hat{\Sigma}^{env}(\omega)$. As discussed above, H_{qp}^{env} directly enters the computation of the one-body terms. In particular, for the onsite term and localized single-QP state ϕ_j we obtain:

$$t_{jj}(\omega) = \left\langle \phi_j | \hat{T} + \hat{V}^{ext} + \hat{\Sigma}^{env}(\omega) | \phi_j \right\rangle, \qquad (8)$$

where $\hat{\Sigma}^{env}$ is the self-energy representing the effective interactions among a QP in the subspace and electrons in the environment. The expectation value of $\hat{T}$ depends only on ϕ_j and hence it is static. Similarly, the external potential ($\hat{V}^{ext}$) is not frequency dependent, though this may be further generalized if the electron-phonon coupling is taken into account. In this picture, the electron-phonon coupling is represented as a charge induced structural reorganization. As such, in the downfolded treatment, the external potential is independent of the electronic configuration, i.e., static. In principle, this constraint may be lifted in a more generalized case when lattice coupling is taken into account. Hence, both $\hat{T}$ and $\hat{V}^{ext}$ capture trivial differences between the subspace sites j. Previously, the definition of the t amplitudes was typically limited only to these two terms[41,42]. In contrast, the self-energy introduces non-trivial dynamical effects. In addition, the method can be extended beyond 0K to include the electronic temperature as explained earlier.

The remaining step to compute the excitation spectrum of the subspace using Eq. (1) is not straightforward if the renormalized interactions remain functions of frequency, i.e., $t(\omega)$ and $W(\omega)$. Since the representation stems directly from the effective downfolding corresponding to one- and two-body propagators, we consider t and W evaluated at ω corresponding to the poles of equilibrium G and L in the frequency domain.

The one-body term is directly linked to the fixed point solution of the QP Hamiltonian, H_{qp}, in which Σ is evaluated directly at the QP energy, ω_{qp}. In general, ω_{qp} differs for the individual cases. e.g., the on-site term t_{jj} and the inter-site single QP propagator t_{ij} are distinct and the effective QP energies (hence ω_{qp}) are thus different. The portion of the self-energy that represents the downfolded environment, Σ^{env}, is also evaluated at ω_{qp}, as discussed e.g., in refs. [15,40]. Since the subspace orbital basis does not diagonalize H_{qp} nor H_{qp}^{env}, the off-diagonal (hopping) terms t_{ij}, are computed as

$$t_{ij} = \frac{1}{4} \left[t_{ij}(\omega_{qp}^i) + t_{ij}(\omega_{qp}^j) + t_{ji}(\omega_{qp}^i) + t_{ji}(\omega_{qp}^j) \right], \qquad (9)$$

where ω_{qp}^i is the ith subspace QP energy. This approach follows the QP-selfconsistent method[43,44] that imposes self-adjointness of the Hamiltonian. In our practical calculations (detailed below) we found that the H_{qp} is still strongly diagonally dominant, i.e., $t_{ii} \gg t_{ij}$ and the symmetrized and hermitized form of t_{ij} is justified in these cases[43,44]. The two-body interactions are renormalized by charge density fluctuations in the remainder of the system, i.e., polarization due to the electron-hole transitions (excitations) in the subspace. In the following, we consider such optical excitations to determine the frequency at which $W_{ijkl}(\omega)$ should be computed (Eq. (6)). Note that this is a particular choice; an alternative strategy is to compute the two-body terms from two-particle propagator, e.g., in the T-matrix approximation[28,48] in which the two-particle interactions are renormalized by particle-particle scattering (which needs to be restricted to the environment). As we are primarily considering the particle-hole screening

in Eq. (5), we employ the Bethe-Salpeter equation for particle-hole propagator L. The excitations are defined as the fixed-point solutions for a two-QP Hamiltonian, H_{2qp}[50], which for a particular set of subspace states is:

$$\langle ij | H_{2qp}(\omega) | kl \rangle = \Delta_{ij} \delta_{ik} \delta_{jl} + \mathcal{K}_{ijkl}(\omega). \qquad (10)$$

Here, $\Delta_{ij} = \omega_{qp}^i - \omega_{qp}^j$ is the difference between two-QP energies, corresponding to two independent single-QP excitations. Further, $\mathcal{K}$ is a general dynamical interaction kernel that couples the two QPs. We consider that the two-body interactions inside the subspace are mediated by the screened Coulomb interaction at the random phase approximation (RPA) level ($\mathcal{K}_{ijkl} = W_{ijkl}^{env}$). This choice is motivated by two reasons: for the description of individual QPs, we resort to the GW approximation (see below) in which we employ RPA; further, this approach directly utilizes the quantity of interest, i.e., $W_{ijkl}(\omega)$ from Eq. (6). The particle-hole excitations ω_{2qp} are found by computing the H_{2qp} as fixed point equation for energy (ω_{2qp}) satisfying Eq. (10). In practice, this is computed numerically through bisection so that $\langle ij | H_{2qp}(\omega) | kl \rangle = \omega_{2qp}$ and $\mathcal{K}_{ijkl}(\omega_{2qp})$ are satisfied simultaneously. Note, each two-quasiparticle propagator differs for each set of $ijkl$. In the following, we assume that the dynamically renormalized two-body interactions are screened (by the polarization of the environment) in the same way as the electron excitations in the subspace. Hence the two-body interactions from Eq. (6) enter the Hamiltonian in Eq. (1) as $W_{ijkl}(\omega_{2qp})$.

Stochastic formalism

We now comment on the practical and efficient implementation of the one and two-body terms. The key ingredient is the renormalized two-body interaction, Eq. (5) which directly enters the evaluation of W_{ijkl} and t (Eqs. (6) and (8)). In practice, we employ a stochastic evaluation of the QP-QP and single-QP terms, i.e., we sample the action of the screened interaction: instead of computing the environment polarizability, χ^{env}, we repeatedly compute the induced density $\delta n^{env} = \chi^{env} \delta U$ constructed from random vectors projected on the occupied portion of the single particle Hilbert space[30,51]. The stochastic occupied states, $|\eta\rangle$, are projected such that they are a part of the weakly correlated environment: $|\tilde{\eta}\rangle = (1 - P_\phi)|\eta\rangle$, where $|\eta\rangle$ spans the entire occupied subspace. Here P_ϕ is the projection operator explicitly formed from the states of the correlated subspace, $\{\phi\}$:

$$P_\phi = \sum_{k \in \{\phi\}} f_k |\phi_k\rangle\langle\phi_k|, \qquad (11)$$

where f_k is the occupation of the kth state. The variation of the charge density, δn is induced by electrons in particular states of the correlated region $\{\phi\}$, which create a perturbing potential at $t = 0$. The density is constructed from random vectors as $n(\mathbf{r}, t) = \lim_{N_\zeta \to \infty} \frac{1}{N_\zeta} \sum_{j=1}^{N_\zeta} |\tilde{\eta}(\mathbf{r}, t)|^2$. In practice, the response is computed separately for each perturbation (i.e., for each set of perturbing states $\{\phi\}$); yet the overall cost is significantly reduced compared to the conventional (deterministic) method as only a few sampling vectors $|\tilde{\eta}\rangle$ are necessary to converge the one- and two-body terms. This is discussed in Supplementary Information Sec. II in more detail. The time evolution of $|\tilde{\eta}\rangle$ states is evaluated in the RPA, in which only the (mean field) ground state Hamiltonian explicitly depends on time only through the Hartree potential[29,30,47,51,52].

For the two-body terms, we conventionally separate the bare and polarization contributions $W_{ijkl}(\omega) = W_{ijkl}^b + W_{ijkl}^p(\omega)$, where the former is directly computed as the static part of Eq. (6), and the latter is obtained by Fourier transformation from its

time-dependent form:

$$\langle \phi_i \phi_j | \tilde{W}^{\mathrm{p}}(t) | \phi_k \phi_l \rangle = \int \phi_i^*(\mathbf{r}) \phi_j(\mathbf{r}) \tilde{u}(\mathbf{r}, t) d\mathbf{r}. \quad (12)$$

We use a time ordered induced potential u, computed from its retarded counterpart: $\tilde{u}^r(1) = v(1, \bar{2}) \delta n^{\mathrm{env}}(\bar{2})$, where the density fluctuation is a response to a perturbation from the correlated subspace. The time-evolved states $|\bar{\eta}\rangle$ are repeatedly projected using P_ϕ at each time step to exclude the dynamics of the correlated subspace. This constitutes the stochastic density constrained RPA (s-cRPA) introduced in Ref. [29]. Note, the time-evolution truncation introduces an effective broadening, which translates into a finite frequency resolution of $W(\omega)$ (see details in Section "Implementation").

Finally, the contribution to the renormalized Hartree self-energy, $\Sigma_{\mathrm{H}}^{\mathrm{env}}$ is similar in nature to Eq. (12), as it also contains the dynamically screened W^{env} term computed via stochastic sampling. However, instead of treating only a set of correlated states $\{\phi\}$, it applies to the interaction between the density of the environment and an individual single-QP density, represented by $|\phi_j(\mathbf{r})|^2$. As such it is part of the one-body t term.

In practical calculations, further approximations need to be introduced for the sake of tractability. As argued earlier, the G_0W_0 approximation, which captures the correlation effects via induced charge density fluctuations, provides a good choice[30–32]. For evaluating the $\Sigma_{\mathrm{xc}}^{\mathrm{env}}$ in the t term, we resort to a formulation analogous to G_0W_0 as well. In practice, this means that $\tilde{\Gamma}^{\mathrm{env}}(1, 2, 3) \approx \delta(1, 2) \delta(1, 3)$. As a result, this form neglects the higher order screening in $\Sigma_{\mathrm{xc}}^{\mathrm{env}}$, that is inherently part of $\bar{\Gamma}$. While this step is an ad-hoc approximation, it still corresponds to the leading-order term capturing the environment exchange-correlation self-energy.

In this approximation, our calculations employ a portion of the G_0W_0 environment exchange-correlation self-energy, which depends only on an underlying mean-field Hamiltonian used to generate the starting point. Analogously to the two-body terms and the Hartree self-energy, $\Sigma_{\mathrm{xc}}^{\mathrm{env}}$ is efficiently evaluated using a real-time propagation of stochastic vectors (sampling the fluctuations in the environment induced by addition of a particle or hole to the subspace). This step follows the stochastic decomposition scheme detailed in ref. [40]. In the space-time representation, $G_0^{\mathrm{env}}(\mathbf{r}, \mathbf{r}', t) = \{\tilde{\xi}^*(t, \mathbf{r}') \tilde{\zeta}(\mathbf{r})\}$, where $|\tilde{\zeta}\rangle$ is obtained from a random state sampling the entire single-particle Hilbert space, $|\zeta\rangle$, by projection $|\tilde{\zeta}\rangle = (1 - P_\phi)|\zeta\rangle$. Further, $|\xi(t)\rangle$ is a random state in either occupied or unoccupied subspace of the environment states (obtained by filtering) which is propagated backward or forward in time due to time ordering applied to holes and particles[30,47,51,52]. Again, only its portion $|\tilde{\xi}\rangle$, which is orthogonal to the correlated subspace, contributes to G^{env} and it is prepared as $|\tilde{\xi}\rangle = P_\phi |\xi\rangle$. Finally, the time evolution is governed by the U_0 which depends only on the ground state non-interacting Hamiltonian and $|\xi(\tilde{t})\rangle = U_0(t)|\tilde{\xi}\rangle$. The practical expression for the xc self-energy for a state ϕ_j in Eq. (8) thus becomes (in the time domain): $\langle \phi_j | \Sigma(t) | \phi_j \rangle = \langle \phi_j \xi(t) | \hat{W}^{\mathrm{env}}(t) | \tilde{\zeta} \phi_j \rangle$.

Implementation

The following calculation workflow was employed in this work:

- The QuantumESPRESSO code[53] code was used to perform the atomic relaxations of the NV⁻ center defect in 3D periodic diamond supercells of size 215, 511 and 999 atoms. The Tkatchenko-Scheffler's total energy corrections[54] and spin polarization were included. The equilibrium lattice parameter of 3.543 Å was used to construct the supercells.
- The starting-point DFT calculations for all systems were performed with a real-space non spin-polarized DFT

implementation, employing regular grids, Troullier-Martins pseudopotentials[55], and the PBE[56] functional for exchange and correlation. For 3D periodic structures to converge the eigenvalues to < 5 meV, we use a kinetic energy cutoff of 26 E_{h}. The real-space grids of $68 \times 68 \times 68$; $92 \times 92 \times 92$; and $112 \times 112 \times 112$ with the spacing of ~ 0.3 a_0 were used for 215, 511, and 999 supercells; Note, the real-space implementation of the stochastic GW methodology requires that instead of sampling the Brillouin zone via k points, we effectively only sample the Γ point for a large supercell. The 512-atom supercell corresponds to the 4x4x4 k-point mesh, and the 4,096 atom supercell corresponds to the 8x8x8 mesh.

- The maximally localized functions were obtained by PMWannier2.0 code based on sequential optimization[36,57]. The localized orbitals were centered on four sites: nitrogen atom and three nearest to vacancy carbon atoms (Fig. 1 of the main text). This is a minimal model of the NV-center that is commonly used[27,42,58] to describe its low-lying excited states.

- Further, the effective parameters were computed in a localized basis. The dynamical renormalization of the parameters was included through the frequency dependent dielectric screening by the host environment containing 1020 valence states. The total number of states (occupied and unoccupied) is given by the real-space grid size that amounts to 778,688 states which are being stochastically sampled. Screening was computed with the s-cRPA method, which was implemented within a development version of the StochasticGW code[29,30,40,51,52]. In cRPA, the polarization of the system is divided into subspace part P^{sub} and the environment part P^{env}. While the former is excluded from the model Hamiltonian, the transition between subspace and the environment ($P^{\mathrm{sub-env}}$), in principle, should be included. We tested both strategies: with and without the transition between the subspace and the environment. Specifically, in the real-time formulation of cRPA, the subspace states are perturbed and propagated, creating density fluctuations in the rest of the system. The time-evolved states can transition between the subspace and rest. If these interactions are to be excluded, we constrain the dynamics by projections at each time step. Our tests showed that both strategies lead in this particular case to the same result for the screening (with sub-1% differences in the final results). In our calculations, we employed in total 3200 samplings for the one and two body terms; a detailed study of the convergence of the stochastic errors is in the Supplementary Information Sec. II. The frequency resolution depends on the time propagation of the induced charge density. Here, it was performed for a maximum propagation time of 50 a.u., with a time-step of 0.05 a.u. The same time propagation was shown to provide well-converged results for bulk diamond in our previous work[30].

- At the next step, we calculated single and double quasiparticle energies ω_{qp} and ω_{2qp} by solving auxiliary quasiparticle Hamiltonian and Bethe-Salpeter equations. At these finite frequencies, $t(\omega_{\mathrm{qp}})$ and $W(\omega_{\mathrm{2qp}})$ parameters enter the effective Hamiltonian Eq. (2).

- Finally, to obtain the set of the many-body excited states in the NV center we performed an exact diagonalization of the effective Hamiltonian.

DATA AVAILABILITY

All the data supporting the results of this study are available upon reasonable request to the corresponding author

CODE AVAILABILITY
The public version of the stochastic GW code is available at stochasticGW.com. We used a development version of the stochastic *GW* to perform calculations, which will be released soon and is available upon reasonable request.

REFERENCES
1. Wagner, L. K. & Ceperley, D. M. Discovering correlated fermions using quantum monte carlo. *Rep. Prog. Phys* **79**, 094501 (2016).
2. Tubman, N. M. et al. Modern approaches to exact diagonalization and selected configuration interaction with the adaptive sampling ci method. *J. Chem. Theory Comput.* **16**, 2139 (2020).
3. Szalay, P. G., Muller, T., Gidofalvi, G., Lischka, H. & Shepard, R. Multiconfiguration self-consistent field and multireference configuration interaction methods and applications. *Chem. Rev.* **112**, 108 (2012).
4. Li, J., Otten, M., Holmes, A. A., Sharma, S. & Umrigar, C. J. Fast semistochastic heat-bath configuration interaction. *J. Chem. Phys.* **149**, 214110 (2018).
5. Blunt, N. et al. Semi-stochastic full configuration interaction quantum monte carlo: Developments and application. *J. Chem. Phys.* **142**, 184107 (2015).
6. Mejuto-Zaera, C. et al. Efficient hybridization fitting for dynamical mean-field theory via semi-definite relaxation. *Phys. Rev. B* **101**, 035143 (2020).
7. Orús, R. Tensor networks for complex quantum systems. *Nat. Rev. Phys.* **1**, 538 (2019).
8. Chan, G. K.-L. & Sharma, S. The density matrix renormalization group in quantum chemistry. *Annu. Rev. Phys. Chem.* **62**, 465 (2011).
9. Georges, A. Strongly correlated electron materials: Dynamical mean-field theory and electronic structure. *AIP Conf. Proc.* **715**, 3 (2004).
10. Libisch, F., Huang, C. & Carter, E. A. Embedded correlated wavefunction schemes: Theory and applications. *Acc. Chem. Res.* **47**, 2768 (2014).
11. Cui, Z.-H., Zhu, T. & Chan, G. K.-L. Efficient implementation of ab initio quantum embedding in periodic systems: Density matrix embedding theory. *J. Chem. Theory Comput.* **16**, 119 (2019).
12. Pham, H. Q., Hermes, M. R. & Gagliardi, L. Periodic electronic structure calculations with the density matrix embedding theory. *J. Chem. Theory Comput.* **16**, 130 (2019).
13. Rusakov, A. A., Iskakov, S., Tran, L. N. & Zgid, D. Self-energy embedding theory (seet) for periodic systems. *J. Chem. Theory Comput.* **15**, 229 (2018).
14. Ma, H., Sheng, N., Govoni, M. & Galli, G. Quantum embedding theory for strongly correlated states in materials. *J. Chem. Theory Comput.* **17**, 2116 (2021).
15. Sheng, N., Vorwerk, C., Govoni, M. & Galli, G. Green's function formulation of quantum defect embedding theory. *J. Chem. Theory Comput.* **18**, 3512–3522 (2022).
16. Dvorak, M. & Rinke, P. Dynamical configuration interaction: Quantum embedding that combines wave functions and green's functions. *Phys. Rev. B* **99**, 115134 (2019).
17. Dvorak, M., Golze, D. & Rinke, P. Quantum embedding theory in the screened coulomb interaction: Combining configuration interaction with g w/bse. *Phys. Rev. Mater.* **3**, 070801 (2019).
18. Hampel, A., Beck, S. & Ederer, C. Effect of charge self-consistency in dft+ dmft calculations for complex transition metal oxides. *Phys. Rev. Res.* **2**, 033088 (2020).
19. Acharya, S. et al. Importance of charge self-consistency in first-principles description of strongly correlated systems. *npj Comput. Mater.* **7**, 1 (2021).
20. Aryasetiawan, F. et al. Frequency-dependent local interactions and low-energy effective models from electronic structure calculations. *Phys. Rev. B* **70**, 195104 (2004).
21. Aryasetiawan, F., Tomczak, J. M., Miyake, T. & Sakuma, R. Downfolded self-energy of many-electron systems. *Phys. Rev. Lett.* **102**, 176402 (2009).
22. Werner, P. & Millis, A. J. Dynamical screening in correlated electron materials. *Phys. Rev. Lett.* **104**, 146401 (2010).
23. Casula, M. et al. Low-energy models for correlated materials: bandwidth renormalization from coulombic screening. *Phys. Rev. Lett.* **109**, 126408 (2012).
24. Sakuma, R., Werner, P. & Aryasetiawan, F. Electronic structure of srvo 3 within g w + dmft. *Phys. Rev. B* **88**, 235110 (2013).
25. Bockstedte, M., Schütz, F., Garratt, T., Ivády, V. & Gali, A. Ab initio description of highly correlated states in defects for realizing quantum bits. *npj Quantum Mater.* **3**, 1 (2018).
26. Ma, H., Govoni, M. & Galli, G. Quantum simulations of materials on near-term quantum computers. *npj Comput. Mater.* **6**, 1 (2020).
27. Muechler, L. et al. Quantum embedding methods for correlated excited states of point defects: Case studies and challenges. *Phys. Rev. B* **105**, 235104 (2022).
28. Martin, R. M., Reining, L., Ceperley, D. M., *Interacting Electrons* (Cambridge University Press, 2016).
29. Romanova, M. & Vlček, V. Stochastic many-body calculations of moiré states in twisted bilayer graphene at high pressures. *npj Comput. Mater.* **8**, 1 (2022).
30. Vlček, V., Li, W., Baer, R., Rabani, E. & Neuhauser, D. Swift GW beyond 10,000 electrons using sparse stochastic compression. *Phys. Rev. B* **98**, 075107 (2018).
31. Löfås, H., Grigoriev, A., Isberg, J. & Ahuja, R. Effective masses and electronic structure of diamond including electron correlation effects in first principles calculations using the gw-approximation. *AIP Adv.* **1**, 032139 (2011).
32. Gao, S.-P. Band gaps and dielectric functions of cubic and hexagonal diamond polytypes calculated by many-body perturbation theory. *Phys. Status Solidi b* **252**, 235 (2015).
33. Rocca, D., Ping, Y., Gebauer, R. & Galli, G. Solution of the bethe-salpeter equation without empty electronic states: Application to the absorption spectra of bulk systems. *Phys. Rev. B* **85**, 045116 (2012).
34. Leng, X., Jin, F., Wei, M. & Ma, Y. Gw method and bethe–salpeter equation for calculating electronic excitations. *Wiley Interdiscip. Rev. Comput. Mol.* **6**, 532 (2016).
35. Mejuto-Zaera, C. et al. Are multi-quasiparticle interactions important in molecular ionization? *J. Chem. Phys.* **154**, 121101 (2021).
36. Weng, G., Romanova, M., Apelian, A., Song, H. & Vlček, V. Reduced scaling of optimal regional orbital localization via sequential exhaustion of the single-particle space. *J. Chem. Theory Comput.* **18**, 4960 (2022).
37. Nebel, C. and Ristein, J., *Thin-Film Diamond I:(part of the Semiconductors and Semimetals Series)* (Academic Press, 2003).
38. Giustino, F., Louie, S. G. & Cohen, M. L. Electron-phonon renormalization of the direct band gap of diamond. *Phys. Rev. Lett.* **105**, 265501 (2010).
39. Botti, S. & Marques, M. A. Strong renormalization of the electronic band gap due to lattice polarization in the g w formalism. *Phys. Rev. Lett.* **110**, 226404 (2013).
40. Romanova, M. & Vlček, V. Decomposition and embedding in the stochastic GW self-energy. *J. Chem. Phys.* **153**, 134103 (2020).
41. Babamoradi, M., Heidari Saani, M., Ranjbar, A., Vesaghi, M. & Kawazoe, Y. Effect of lattice relaxation on spin density of nitrogen-vacancy centers in diamond and oscillator strength calculations. *Eur. Phys. J. B* **84**, 1 (2011).
42. Ranjbar, A. et al. Many-electron states of nitrogen-vacancy centers in diamond and spin density calculations. *Phys. Rev. B* **84**, 165212 (2011).
43. Faleev, S. V., Van Schilfgaarde, M. & Kotani, T. All-electron self-consistent GW approximation: Application to Si, MnO, and NiO. *Phys. Rev. Lett.* **93**, 126406 (2004).
44. Bruneval, F., Vast, N. & Reining, L. Effect of self-consistency on quasiparticles in solids. *Phys. Rev. B* **74**, 045102 (2006).
45. Davies, G. & Hamer, M. Optical studies of the 1.945 ev vibronic band in diamond. *Proc. R. Soc. Lond. A Math. Phys. Sci.* **348**, 285 (1976).
46. Acosta, V., Jarmola, A., Bauch, E. & Budker, D. Optical properties of the nitrogen-vacancy singlet levels in diamond. *Phys. Rev. B* **82**, 201202 (2010).
47. Vlcek, V. Stochastic vertex corrections: Linear scaling methods for accurate quasiparticle energies. *J. Chem. Theory Comput.* **15**, 6254 (2019).
48. Mejuto-Zaera, C. & Vlcek, V. Self-consistency in $gw\Gamma$ formalism leading to quasiparticle-quasiparticle couplings. *Phys. Rev. B* **106**, 165129 (2022).
49. Hedin, L. New method for calculating the one-particle green's function with application to the electron-gas problem. *Phys. Rev.* **139**, A796 (1965).
50. Onida, G., Reining, L. & Rubio, A. Electronic excitations: density-functional versus many-body green's-function approaches. *Rev. Mod. Phys.* **74**, 601 (2002).
51. Neuhauser, D. et al. Breaking the theoretical scaling limit for predicting quasi-particle energies: The stochastic GW approach. *Phys. Rev. Lett.* **113**, 076402 (2014).
52. Vlček, V., Rabani, E., Neuhauser, D. & Baer, R. Stochastic GW calculations for molecules. *J. Chem. Theory Comput.* **13**, 4997 (2017).
53. Giannozzi, P. et al. Advanced capabilities for materials modelling with quantum espresso. *J. Condens. Matter Phys.* **29**, 465901 (2017).
54. Tkatchenko, A. & Scheffler, M. Accurate molecular van der waals interactions from ground-state electron density and free-atom reference data. *Phys. Rev. Lett.* **102**, 073005 (2009).
55. Troullier, N. & Martins, J. L. Efficient pseudopotentials for plane-wave calculations. *Phys. Rev. B* **43**, 1993 (1991).
56. Perdew, J. P. & Wang, Y. Accurate and simple analytic representation of the electron-gas correlation energy. *Phys. Rev. B* **45**, 13244 (1992).
57. Weng, G. & Vlček, V. Efficient treatment of molecular excitations in the liquid phase environment via stochastic many-body theory. *J. Chem. Phys.* **155**, 054104 (2021).
58. Choi, S., Jain, M. & Louie, S. G. Mechanism for optical initialization of spin in nv-center in diamond. *Phys. Rev. B* **86**, 041202 (2012).
59. Towns, J. et al. Xsede: Accelerating scientific discovery. *Comput. Sci. Eng.* **16**, 62 (2014).

ACKNOWLEDGEMENTS

AUTHOR CONTRIBUTIONS

M.R., A.A., and G.W. conducted the research work under the guidance of V.V. All authors contributed and reviewed the manuscript.

COMPETING INTERESTS

The authors declare no competing interests.

ADDITIONAL INFORMATION

Supplementary information The online version contains supplementary material available at https://doi.org/10.1038/s41524-023-01078-5.

Correspondence and requests for materials should be addressed to Vojtěch Vlček.

Reprints and permission information is available at http://www.nature.com/reprints

Publisher's note Springer Nature remains neutral with regard to jurisdictional claims in published maps and institutional affiliations.